Front. Optoelectron. 2021, 14(3): 298–310
https://doi.org/10.1007/s12200-020-1033-z

RESEARCH ARTICLE

$Li_xNa_{2-x}W_4O_{13}$ nanosheet for scalable electrochromic device

Yucheng LU[1*], Xin YANG[2*], Hongrun JIN[1], Kaisi LIU[1], Guoqun ZHANG[1], Liang HUANG[1], Jia LI (✉)[2], Jun ZHOU (✉)[1]

1 Wuhan National Laboratory for Optoelectronics, Huazhong University of Science and Technology, Wuhan 430074, China
2 Shenzhen Geim Graphene Center, Tsinghua Shenzhen International Graduate School, Tsinghua University, Shenzhen 518055, China

© Higher Education Press 2020

Abstract The printed electronics technology can be used to efficiently construct smart devices and is dependent on functional inks containing well-dispersed active materials. Two-dimensional (2D) materials are promising functional ink candidates due to their superior properties. However, the majority 2D materials can disperse well only in organic solvents or in surfactant-assisted water solutions, which limits their applications. Herein, we report a lithium (Li)-ion exchange method to improve the dispersity of the $Na_2W_4O_{13}$ nanosheets in pure water. The Li-ion-exchanged $Na_2W_4O_{13}$ ($Li_xNa_{2-x}W_4O_{13}$) nanosheets show highly stable dispersity in water with a zeta potential of −55 mV. Moreover, this aqueous ink can be sprayed on various substrates to obtain a uniform $Li_xNa_{2-x}W_4O_{13}$ nanosheet film, exhibiting an excellent electrochromic performance. A complementary electrochromic device containing a $Li_xNa_{2-x}W_4O_{13}$ nanosheet film as an electrochromic layer and Prussian white (PW) as an ion storage layer exhibits a large optical modulation of 75% at 700 nm, a fast switching response of less than 2 s, and outstanding cyclic stability. This $Na_2W_4O_{13}$-based aqueous ink exhibits considerable potential for fabricating large-scale and flexible electrochromic devices, which would meet the practical application requirements.

Keywords printed electronics technology, two-dimensional material, ink, ion exchange, electrochromic device

1 Introduction

The printed electronics technology has drawn increasing attention in previous decades as a promising deposition technology [1,2]; some examples of such technologies include spray coating [3,4], inkjet printing [5,6], and screen printing [7,8]. The aforementioned solution-based deposition methods allow the low-cost preparation of large-area, flexible, or patterned devices. In this technology, one of the most important factors is the usage of functional inks containing a well-dispersed active material, which demand the vigorous development of materials science [9–12].

Two-dimensional (2D) materials with unique structural properties exhibit superior performance with respect to various applications such as energy storage [13,14], optoelectronics [15,16], and catalysis [17,18]. Moreover, when combined with the printed electronics technology, 2D materials can easily construct functional devices, including transistors [19,20], supercapacitors [21], and light-emitting diodes (LEDs) [22], in a fast and simple manner. Thus, studies on inks containing 2D materials should not be neglected owing to the promising demonstration of the liquid-phase exfoliation of 2D materials such as graphene [23], MXenes [24], transition metal dichalcogenides (TMDs) [25], and transition metal oxides (TMOs) [26]. Typically, 2D materials can be stabilized in organic solvents, the surface energies of which match with those of 2D materials [23]. However, organic solvents are often toxic and costly. Water is considered to be an ideal solvent for preparing ink because it is environmentally friendly, inexpensive, and abundant. Generally, 2D materials require the assistance of surfactants to disperse well in water [27]. However, the surfactants on their surface are difficult to remove, which probably limits the performance of the devices. Therefore, exploring an efficient methodology to directly disperse 2D materials in water is essential for the development of 2D material inks.

Tungsten oxide (WO_3) having several outstanding properties is a promising material for electrochromic [28,29], sensing [30], and catalytic [31] applications. Nevertheless, few studies have investigated 2D WO_3-based aqueous inks. Liang et al. prepared an aqueous dispersion of $WO_3 \cdot H_2O$ nanosheets through the ultrasonic

Received March 31, 2020; accepted April 24, 2020

E-mails: li.jia@sz.tsinghua.edu.cn, jun.zhou@mail.hust.edu.cn

*These authors contributed equally to this work.

exfoliation of bulk $WO_3 \cdot 2H_2O$ in N,N-dimethylformamide (DMF), which considerably increased the complexity of the preparation process [32]. Herein, we report a novel strategy for improving the dispersity of the $Na_2W_4O_{13}$ nanosheets in pure water via the Li-ion exchange method. The partially Li-ion-exchanged $Na_2W_4O_{13}$ ($Li_xNa_{2-x}W_4O_{13}$) nanosheets show a highly stable dispersity in water with a zeta potential of -55 mV. Moreover, this aqueous ink can be sprayed on various substrates to obtain a uniform $Li_xNa_{2-x}W_4O_{13}$ nanosheet film, exhibiting an excellent electrochromic performance. The electrochromic device assembled using a Prussian white (PW) film and a sprayed $Li_xNa_{2-x}W_4O_{13}$ nanosheet film exhibits large optical modulation, fast switching response, and considerable cyclic stability.

2 Experimental section

Synthesis of $Na_2W_4O_{13}$ nanosheets: $Na_2W_4O_{13}$ nanosheets were synthesized using the molten salt method [14]. 5 g of sodium nitrate ($NaNO_3$) was added to a crucible and transferred to a muffle furnace at a temperature of 350°C. When $NaNO_3$ was completely melted, 0.2 g of ammonium tungstate hydrate ($H_{40}N_{10}O_{41}W_{12} \cdot xH_2O$) powder was added into molten $NaNO_3$ for approximately 1 min. Then, the crucible was removed from the muffle furnace and cooled to room temperature. Finally, the $Na_2W_4O_{13}$ nanosheets were collected via vacuum filtration after soaking and washing in deionized (DI) water and drying at 70°C.

Preparation of the $Li_xNa_{2-x}W_4O_{13}$ nanosheet aqueous ink: $Li_xNa_{2-x}W_4O_{13}$ nanosheets were prepared in two steps. Typically, 40 mg of the $Na_2W_4O_{13}$ nanosheets was added to 40 mL of the 1 mol/L lithium sulfate (Li_2SO_4) aqueous solution under stirring for 3–7 days at room temperature. After vacuum filtering the suspension and washing it several times using DI water, $Li_xNa_{2-x}W_4O_{13}$ nanosheets were obtained. Then, this obtained product was dispersed in DI water by probe sonication and centrifuged at 2000 r/min to prepare the $Li_xNa_{2-x}W_4O_{13}$ nanosheet aqueous ink.

Fabrication of the $Li_xNa_{2-x}W_4O_{13}$ nanosheet film: The $Li_xNa_{2-x}W_4O_{13}$ nanosheet film was prepared on fluorine-doped tin oxide (FTO) glass and flexible indium tin oxide (ITO) substrate by spray coating. The $Li_xNa_{2-x}W_4O_{13}$ nanosheet ink was sprayed on the substrate maintained at a temperature of 100°C.

Fabrication of the PW film: The Prussian blue (PB) film was electrodeposited on FTO glass via galvanostatic deposition using a 0.01 mol/L $K_3[Fe(CN)]_6$, 0.01 mol/L $FeCl_3$, and 0.05 mol/L KCl aqueous solution as the electrolyte [33]. Electrochemical deposition was performed under a constant current density of -50 μA/cm^2 for 120 s using clean FTO glass or flexible ITO substrates as the working electrode, a carbon rod as the counter electrode, and Ag/AgCl as the reference electrode. The PW film was obtained from the PB film from a 1 mol/L $LiClO_4$/propylene carbonate (PC) solution.

Assembly of the electrochromic device: The electrochromic device was assembled using the sprayed $Li_xNa_{2-x}W_4O_{13}$ nanosheet film as the electrochromic layer, PW film as the ion storage layer, and a 1 mol/L $LiClO_4$/PC solution as the electrolyte. These two functional layers were separated by a narrow tape at the edges and sealed using epoxy glue.

Characterization: The crystal structure of the materials was determined by X-ray diffraction (XRD) using Cu Kα radiation (λ = 1.5418 Å) (X'Pert Pro, PANalytical). The zeta potential was measured using a Zetasizer (Nano ZSP, Malvern Instruments Limited, UK). Field-emission scanning electron microscopy (FE-SEM, FEI Nova 450 Nano) and transmission electron microscopy (Titan G2 60-300) were employed to explore the structure and morphology of the materials. The chemical composition and oxidized state of materials were studied using X-ray photoelectron spectroscopy (XPS, ESCALab 250). The atomic ratio of the elements and concentration of the dispersions were measured using inductively coupled plasma optical emission spectrometry (ICP–OES, Optima 4300DV). The optical spectrum and *in situ* transmittance response were obtained using a UV spectrophotometer (Shimadzu UV-3600Plus), and the electrochemical tests of electrochromic performance were performed using CHI660D.

Density functional theory calculations: All the density functional theory calculations were performed using the projected augmented wave method and Perdew–Burke–Ernzerhof (PBE) functional within the generalized gradient approximation, as implemented in the Vienna *ab initio* Simulation Package (VASP) [34–37]. The energy cutoff for plane wave expansion was set to 650 eV. All the surfaces were simulated using the slab model. And the same terminations were modelled at the top and bottom of the slab. The atoms in the middle five, two, three, and three layers of (001), (100), (011), and $(01\bar{1})$ facets were fixed at their optimal bulk positions, respectively, whereas the remaining atoms were fully relaxed until the force on each atom was less than 0.02 eV/Å. An implicit solvation model was employed to simulate the water solvent in experiments [38]. The surface energies and interfacial energies were calculated using

$$\gamma = \frac{E_{\text{slab}} - E_{\text{bulk}} - n_{\text{o}}\mu_{\text{o}} - n_{\text{metal}}\mu_{\text{metal}}}{2A},$$

where E_{slab} is the energy of the entire slab, E_{bulk} is the energy of the corresponding bulk phase, A is the surface area of the slab, n_{o} is the number of oxygen atoms in the system, μ_{o} is half the total energy of the oxygen molecule, n_{metal} is the number of metal atoms in the system, and μ_{metal} is the energy per atom of the bulk metal.

3 Results and discussion

3.1 Li-ion-exchanged $Na_2W_4O_{13}$ nanosheets

The Li-ion exchange process is illustrated in Fig. 1(a). The $Na_2W_4O_{13}$ nanosheets (Fig. S1) were synthesized using the molten salt method, as described in a previous study [14]. Li-ion exchange could occur with the addition of $Na_2W_4O_{13}$ nanosheets into the Li_2SO_4 solution, which was under stirring for several days. The Li-ion-exchanged sample was collected by vacuum filtration after being extensively soaked and washed using DI water, which was followed by drying at 70°C. The dispersity of the $Na_2W_4O_{13}$ nanosheets in DI water significantly improved after the Li-ion exchange process. Figure 1(b) shows the optical image of the ink of pristine $Na_2W_4O_{13}$ and $Li_xNa_{2-x}W_4O_{13}$ having the same concentration of 1 mg/mL. The dispersion of $Li_xNa_{2-x}W_4O_{13}$ is more transparent with a strong Tyndall effect owing to the nanosize of the material, which suggests better dispersibility than the pristine $Na_2W_4O_{13}$. Furthermore, the sedimentation curves of suspension when the same initial concentration of 2 mg/mL is considered are shown in Fig. 1(c). Figure 1(c) shows that the concentration of the pristine $Na_2W_4O_{13}$ nanosheets decreased to become less than 0.8 mg/mL after three days, whereas the concentration of the $Li_xNa_{2-x}W_4O_{13}$ nanosheets became greater than 1.2 mg/mL after only two weeks. This improved dispersity of the $Li_xNa_{2-x}W_4O_{13}$ nanosheets in DI water was further confirmed based on the enhanced zeta potential (Fig. 1(d)). According to the Derjaguin-Landau-Verwey-Overbeek (DLVO) theory on colloid stability, the dispersed

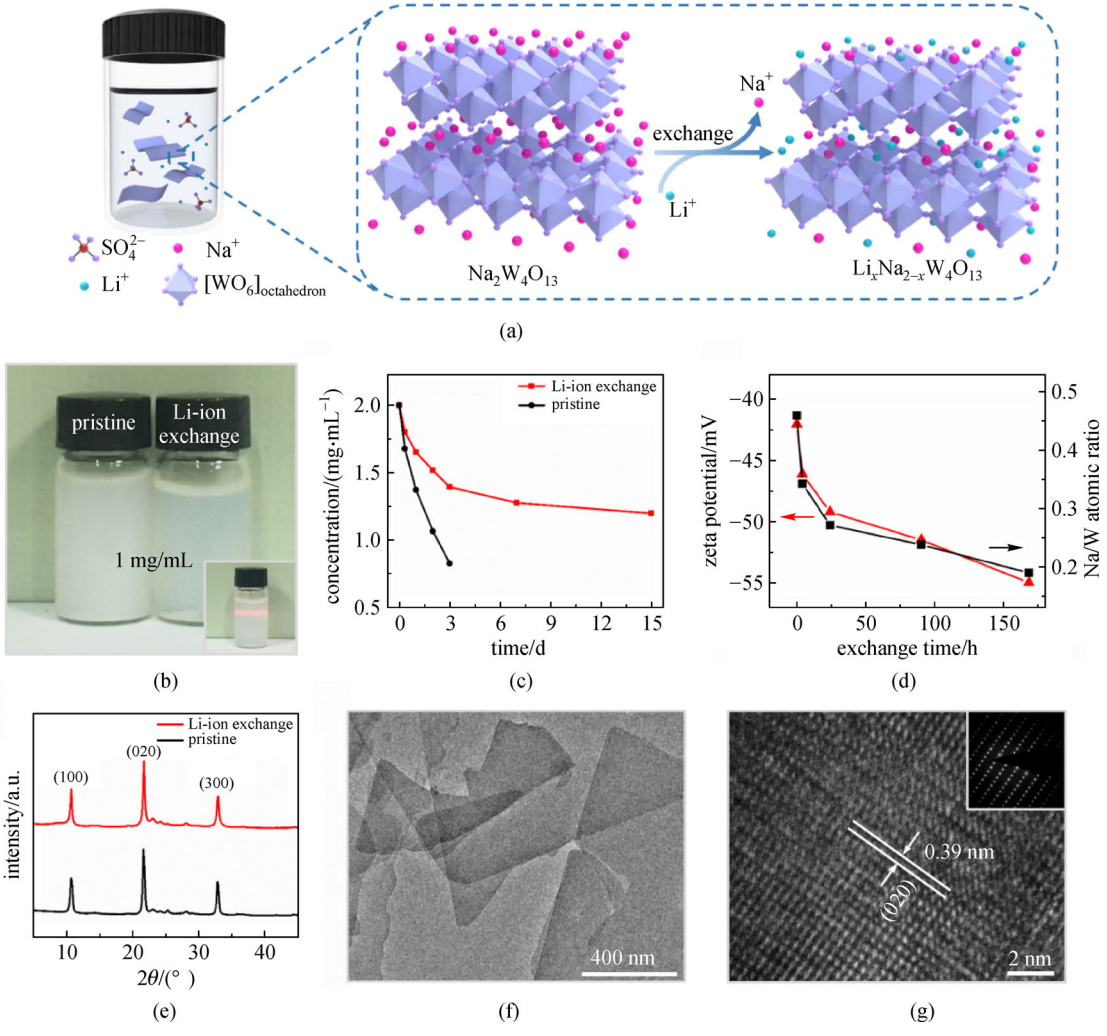

Fig. 1 (a) Schematic of the Li-ion exchange process for the $Na_2W_4O_{13}$ nanosheets. (b) Photographs of the pristine and $Li_xNa_{2-x}W_4O_{13}$ nanosheets dispersed in DI water with a concentration of 1 mg/mL (inset: demonstration of the Tyndall effect with respect to the dispersion of Li-ion-exchanged nanosheets). (c) Sedimentation curves of the pristine $Li_xNa_{2-x}W_4O_{13}$ nanosheets dispersed in DI water with an initial concentration of 2 mg/mL. (d) Dependence of the atomic ratio of sodium compared with that of tungsten (black) and zeta potential in DI water (red) of the $Li_xNa_{2-x}W_4O_{13}$ nanosheets on the Li-ion exchange time. (e) XRD patterns of the pristine $Li_xNa_{2-x}W_4O_{13}$ nanosheets. (f) TEM image of the $Li_xNa_{2-x}W_4O_{13}$ nanosheets. (g) HRTEM and SAED images of the $Li_xNa_{2-x}W_4O_{13}$ nanosheets

nanosheets, which can be considered to be nanoparticles, do not undergo aggregation because of the sufficient electrostatic repulsive force caused by the electric double layer around the nanosheets [39,40]. The resultant repulsion is generally characterized by the zeta potential. As shown in Fig. 1(d), with an increase in the Li-ion exchange time, the zeta potential of the modified nanosheets decreased from −42 to −55 mV, indicating the improved dispersity in water. The atomic ratio of sodium and tungsten in these samples gradually decreased from 0.46 to 0.19, which was determined by following the Li-ion exchange process based on the inductively coupled plasma optical emission spectroscopy (ICP–OES) analysis. Moreover, the total content of alkali metal ions (Li and Na) in these samples remained the same as that of the initial $Na_2W_4O_{13}$ (Fig. S2), which indicated that the exchanged Li ions in the sample improve the dispersity.

XRD was employed to identify the crystal structure of $Na_2W_4O_{13}$ during the Li-ion exchange process (Fig. 1(e)). There is no difference between the XRD patterns of pristine $Na_2W_4O_{13}$ and $Li_xNa_{2-x}W_4O_{13}$, and the diffraction peaks are consistent with those of $Na_2W_4O_{13}$ (JCPDS: 21-1167). The morphology of these samples was explored by scanning electron microscopy (SEM) and transmission electron microscopy (TEM). Figures 1(f) and S3 show that $Li_xNa_{2-x}W_4O_{13}$ retained its original 2D morphology. Moreover, the high-resolution transmission electron microscopy (HRTEM) and selected area electron diffraction (SEAD) images show the regular atomic arrangement and good crystallinity of the $Li_xNa_{2-x}W_4O_{13}$ nanosheets (Fig. 1(g)). XPS was performed to investigate the oxidized state of the $Li_xNa_{2-x}W_4O_{13}$ nanosheets. Figure S4 shows the high-resolution XPS spectrum of the W4f peak. The spin-orbit doublets in the spectrum correspond to the W4f 7/2 and W4f 5/2 peaks, which are located at 35.6 and 37.8 eV, respectively, indicating that W is at the highest oxidized state (W^{6+}) [41].

3.2 Density functional theory calculations

Density functional theory (DFT) calculations were used to elucidate the improved dispersity of the Li-ion exchanged $Na_2W_4O_{13}$ nanosheets in DI water. First, the formation energies of the stable $Li_xNa_{2-x}W_4O_{13}$ structures were determined using the convex hull method, as implemented in the Clusters Approach to Statistical Mechanics (CASM) [42,43] package (Fig. 2(a)). Specifically, a total of 8688 symmetrically distinct $Li_xNa_{2-x}W_4O_{13}$ structures were considered in our calculation, among which the formation energies of 175 configurations (denoted as blue solid circles in Fig. 2(a)) were obtained via DFT calculations, whereas those of the remaining 8513 configurations (denoted as black empty circles in Fig. 2(a)) were predicted using the cluster expansion method. Thus, only one stable Li-ion exchanged structure having a composition of $Li_{1.333}Na_{0.666}W_4O_{13}$ was predicted, as illustrated in Fig. 2(a). The lowest formation energies of different Li-ion exchanged $Li_xNa_{2-x}W_4O_{13}$ configurations at each Li concentration were less than zero, indicating that the exchange of Na ions with Li ions in the $Na_2W_4O_{13}$ nanosheets was energetically favorable, as demonstrated experimentally.

The good dispersity of the as-prepared samples in water mainly depends on the stable interface of the exposed surfaces of nanoparticles and water. The interfacial energy can be used to evaluate the dispersity of the nanosheets in water; a low interfacial energy indicates the good dispersity of nanosheets in water and vice versa. Thus, we investigated the interfacial features of pristine $Na_2W_4O_{13}$ and $Li_2W_4O_{13}$ in water and compared their

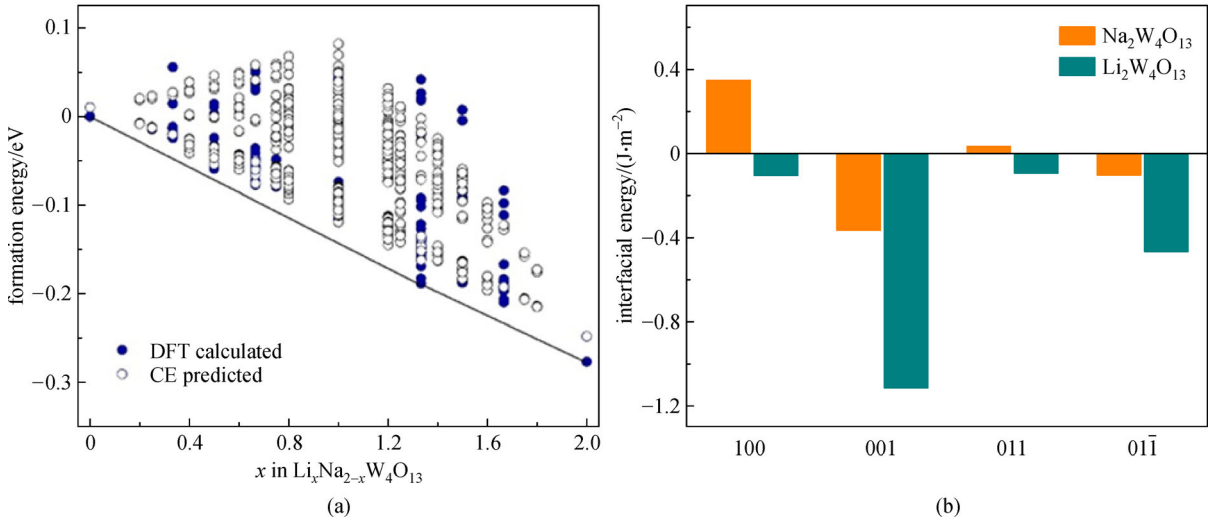

Fig. 2 (a) Formation energies per formula unit versus the fractional lithium concentration in $Li_xNa_{2-x}W_4O_{13}$. The convex hull (tie line) is constructed by jointing the stable structures obtained by the searches. (b) Interfacial energies of four low-index facets of $Na_2W_4O_{13}$ and $Li_2W_4O_{13}$ with favorable terminations in water

corresponding interfacial energies with respect to water by employing the implicit solvation scheme. Four low-index facets of pristine $Na_2W_4O_{13}$, i.e., (001), (100), (011), and (01$\bar{1}$), were considered to completely evaluate the stability of the interface. The favorable termination of these facets was determined by the surface energies in vacuum, as shown in Fig. S5 and Table S1. Based on the favorable termination of four facets in case of pristine $Na_2W_4O_{13}$, we obtained four low-index facets of $Li_2W_4O_{13}$ having the same terminations (Fig. S6). In case of all the considered facets of $Na_2W_4O_{13}$ and $Li_2W_4O_{13}$, the outermost layers comprised alkali metal ions, which would be directly exposed to water. With the introduction of water, the interfacial energies of the $Li_2W_4O_{13}$ surfaces were less than those of the $Na_2W_4O_{13}$ surfaces with respect to the same low-index facets (Fig. 2(b) and Table S2). Because identical facets and relevant terminations were considered for $Li_2W_4O_{13}$ and $Na_2W_4O_{13}$, the interfaces of $Li_2W_4O_{13}$ may be stabilized by the high affinity of Li ions with respect to water. This is particularly important in case of $Na_2W_4O_{13}$ owing to the exchange of Li ion with Na ion, which results in the excellent dispersity of the $Li_xNa_{2-x}W_4O_{13}$ nanosheets in water, as observed experimentally.

3.3 Sprayed $Li_xNa_{2-x}W_4O_{13}$ nanosheet film

Because the $Li_xNa_{2-x}W_4O_{13}$ nanosheets can disperse well in DI water, the $Li_xNa_{2-x}W_4O_{13}$ dispersion can be used as a functional ink in case of the printed electronics technology. A uniform $Li_xNa_{2-x}W_4O_{13}$ nanosheet film coating was obtained on the substrate when this ink was directly sprayed on a hot substrate (Fig. 3(a)). As shown in Fig. 3(b), the $Li_xNa_{2-x}W_4O_{13}$ nanosheets can be clearly observed in the top-view SEM image of the film on the FTO glass. In addition, the cross-section view SEM image (Fig. 3(c)) reveals that the $Li_xNa_{2-x}W_4O_{13}$ nanosheets are compactly stacked on the FTO glass and form a film with a relatively uniform thickness of 350 nm. The as-obtained film exhibits an extremely high optical transmittance of ~90% (the transmittance of the FTO glass is used as the baseline). In addition, the film has strong adhesion to substrate; even the tape fails to damage the film.

WO_3 is a classic electrochromic material because of its large optical tunability in the visible range and excellent cyclic stability [28,44]. The $Li_xNa_{2-x}W_4O_{13}$ nanosheets assembled into a highly transparent film can serve as a promising electrode for electrochromic devices. The electrochromic performance of the sprayed

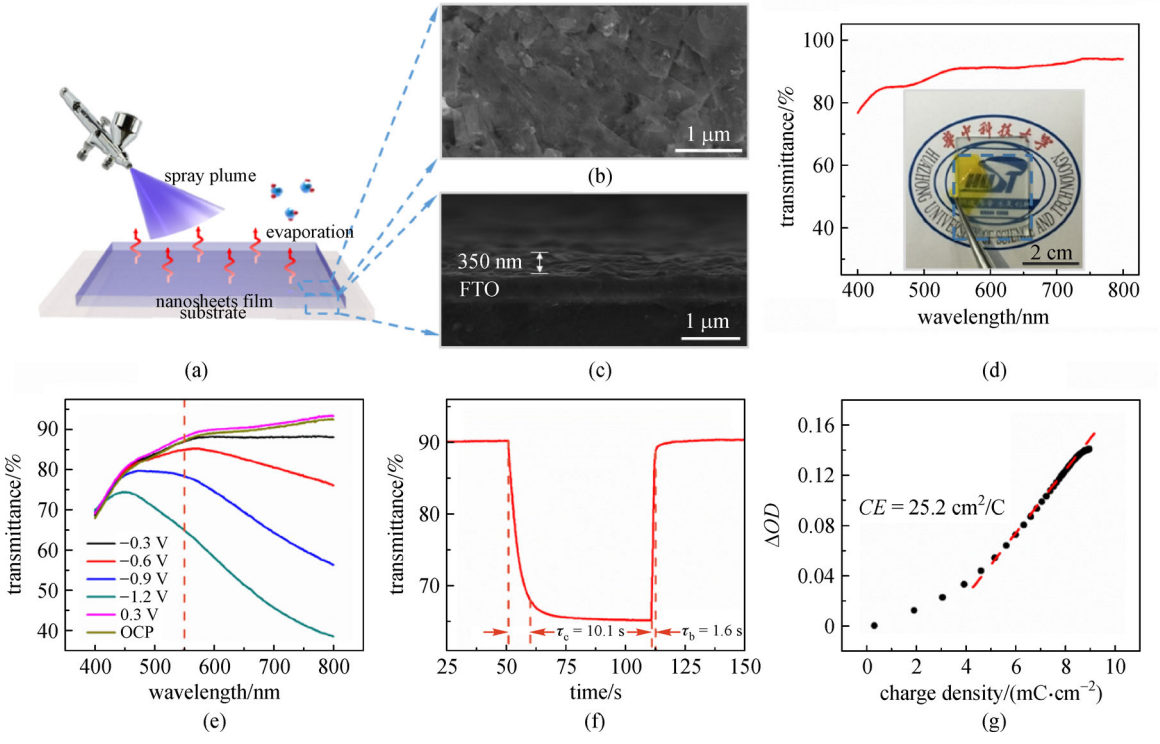

Fig. 3 (a) Schematic of the spray coating process for the $Li_xNa_{2-x}W_4O_{13}$ nanosheet ink. (b) Top-view SEM image of the sprayed $Li_xNa_{2-x}W_4O_{13}$ nanosheet film. (c) Cross-sectional view SEM image of the sprayed $Li_xNa_{2-x}W_4O_{13}$ nanosheet film. (d) Transmittance spectra of the $Li_xNa_{2-x}W_4O_{13}$ nanosheet film in the visible range (inset: photograph of $Li_xNa_{2-x}W_4O_{13}$ nanosheet film electrode). (e) Transmittance spectrum of the $Li_xNa_{2-x}W_4O_{13}$ nanosheet film under different potentials. (f) *In situ* optical switching response of the $Li_xNa_{2-x}W_4O_{13}$ nanosheet film at 550 nm. (g) *In situ* variation of the optical density (ΔOD) at 550 nm versus the charge density for the $Li_xNa_{2-x}W_4O_{13}$ nanosheet film

$Li_xNa_{2-x}W_4O_{13}$ nanosheet film was evaluated in a three-terminal electrochemical cell, where the $Li_xNa_{2-x}W_4O_{13}$ nanosheet film on FTO was considered to be the working electrode, a Pt plate was considered to be the counter electrode, Ag/AgCl was considered to be the reference electrode, and 1 mol/L $LiClO_4$/PC was considered to be the electrolyte. As shown in Fig. 3(e), the transmittance spectra of the $Li_xNa_{2-x}W_4O_{13}$ nanosheet film in the visible range were obtained with respect to the applied potentials; the transmittance of the FTO glass in an electrolyte is considered to be the baseline. With increasing negative potential, the color of the film became deeper blue. The contract at 700 nm is approximately 45% under a potential of -1.2 V; the film bleached to denote initial transmittance under a potential of 0.3 V (Fig. S7). The colored state of the sprayed film was uniform, indicating the uniform distribution of the $Li_xNa_{2-x}W_4O_{13}$ nanosheets.

The switching response (τ_a/τ_b), which is a key parameter with respect to an electrochromic material, is defined as the time required change the total optical modulation by 90% during the coloration or bleaching processes. Because human eyes are most sensitive to a wavelength of approximately 550 nm, the *in situ* transmittance response was measured at 550 nm. The $Li_xNa_{2-x}W_4O_{13}$ nanosheet film exhibited a fast switching response of 10.1/1.6 s for the coloration/bleaching process (Fig. 3(f)). The fast switching response benefits from the reduced ion diffusion paths and the increased Li-ion coefficient because of the morphology of nanosheets, which possess a large specific surface area and have more diffusible channels [45,46]. The asymmetric response result of the conductivity variation of the $Li_xNa_{2-x}W_4O_{13}$ film during the electrochromic process can be obtained from the current curve (Fig. S8). In general, tungsten oxide is more conductive in the colored state (reduced state) accompanied by Li-ion intercalation [45,47].

Another crucial parameter for evaluating the electrochromic performance is the coloration efficiency (*CE*), which is defined as the change in optical density (ΔOD) per unit charge (ΔQ) inserted or extracted from the electrochromic material and can be calculated as follows:

$$CE = \Delta OD/\Delta Q = \lg(T_b/T_c)/\Delta Q,$$

where T_b and T_c refer to the transmittances of the electrochromic material in bleached and colored states, respectively. The relation of ΔOD to the charge density at 550 nm is shown in Fig. 3(g). The *CE* value for the spayed $Li_xNa_{2-x}W_4O_{13}$ nanosheet film calculated based on the slope of the curve is 25.2 cm^2/C.

3.4 Assembly of electrochromic device

Typically, electrochromic devices comprise an electrochromic layer, an ion storage layer, an electrolyte layer, and a conductive layer. Here, we use the $Li_xNa_{2-x}W_4O_{13}$ nanosheet film as the electrochromic layer and PW as the ion storage layer to assemble a complementary electrochromic device (Fig. 4(a)). The electrolyte used for this device is 1 mol/L $LiClO_4$ in the PC solution. Moreover, the PW film can serve as an anodic coloring electrochromic material, and the reversible switch between transparency (PW, reduced state) and blue color (PB, oxidized state) can considerably improve the electrochromic performance of the device. The PW film on the FTO substrate was fabricated by reducing the galvanostatically deposited PB film (Fig. S9). The modulation of transmittance spectra of the electrochromic device (2 cm × 2.5 cm) in the visible range was evaluated with respect to the applied voltages (Fig. 4(d)), where the transmittance of the two FTO glasses sandwiching the electrolyte was considered to be the baseline. The electrochromic device becomes dark blue at a voltage of -2 V (Fig. 4(c)), and the contract at 700 nm reaches ~75%. The bleached state of the electrochromic device can be observed at a voltage of 1 V (Fig. 4(b)), the transmittance of which reaches almost 90% in the visible range. In this case, the switching response and coloration efficiency are superior to those of the sprayed $Li_xNa_{2-x}W_4O_{13}$ film-based single electrochromic electrode. The coloration time and bleaching time of this electrochromic device are 2 and 1.4 s, respectively (Fig. 4 (f), Video S1). The plot of ΔOD variation at 550 nm versus the considered charge density is shown in Fig. 4(g), which shows a coloration efficiency of 67.2 cm^2/C. The cycling stability of this device was tested by the *in situ* transmittance response at cyclic bias voltages of -2 and 1 V. As shown in Fig. 4(e), the contact at 550 nm of the electrochromic device is maintained at ~40% for more than 20000 s (over 1000 cycles), indicating that the electrochemical performance of the device is extremely stable. Figure S10 shows the detailed switching response of the device during the first 10 cycles and after 1000 cycles.

The solution-based deposition technology shows unique advantages with respect to the manufacturing of large-scale and flexible devices without requiring extremely harsh vacuum and gas atmospheres or expensive equipment. The $Li_xNa_{2-x}W_4O_{13}$ nanosheet-based ink can be easily scaled up using the facile molten salt method and the Li-ion exchange strategy. This approach exhibits considerable potential for the preparation of large-size devices. Figure S11 shows rigid and flexible electrodes having sizes of 10 cm × 10 cm and 3 cm × 4 cm, respectively, which were fabricated by spraying this ink on the FTO glass and the flexible ITO substrates. A large-area electrochromic smart window was constructed based on these electrodes. As shown in Figs. 5(a) and 5(b), a smart window (9 cm × 10 cm) can reversibly switch between dark blue and transparency based on the coloration and bleaching responses (Video S2). Figure S12(a) shows the dual-band electrochromic modulation [48–50] of the prototype device. Under a voltage of 1 V, the electrochromic device

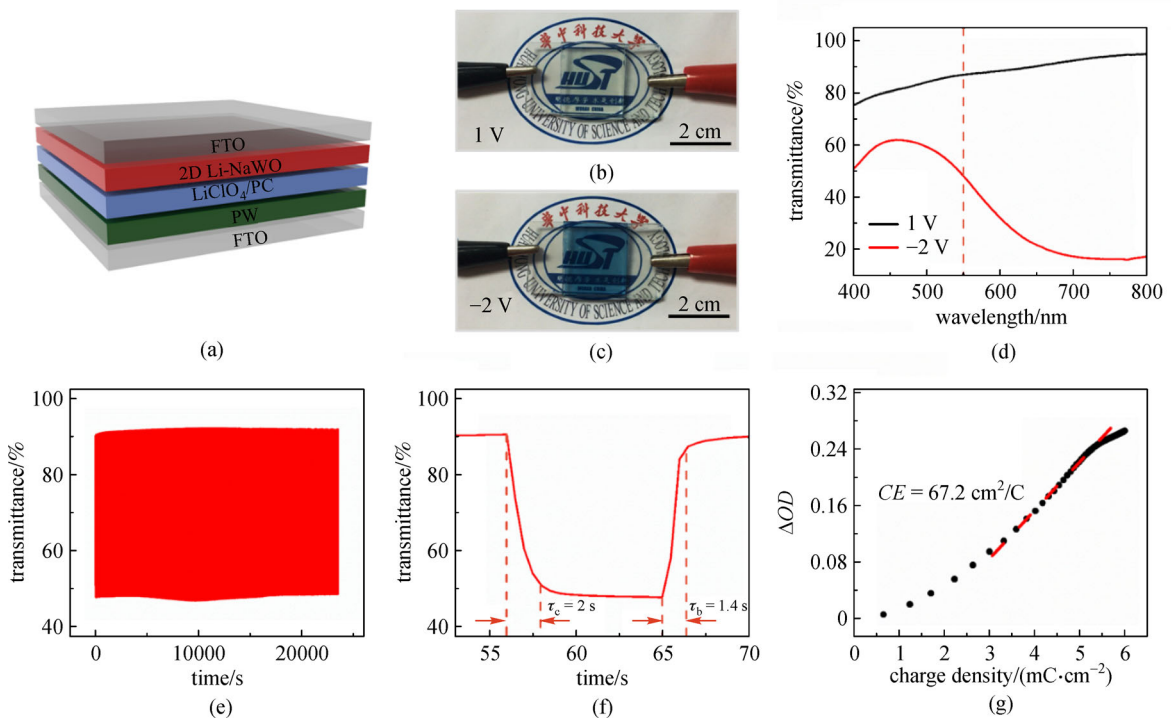

Fig. 4 (a) Schematic of the complementary electrochromic device. (b) Bleaching state of the electrochromic device under a voltage of 1 V. (c) Coloration state of the electrochromic device under a voltage of –2 V. (d) Transmittance spectrum of the electrochromic device under different voltages. (e) *In situ* transmittance at 550 nm for the measurement of cyclic stability. (f) *In situ* optical switching response of the electrochromic device at 550 nm. (g) *In situ* variation of the optical density (ΔOD) at 550 nm versus the charge density for the electrochromic device

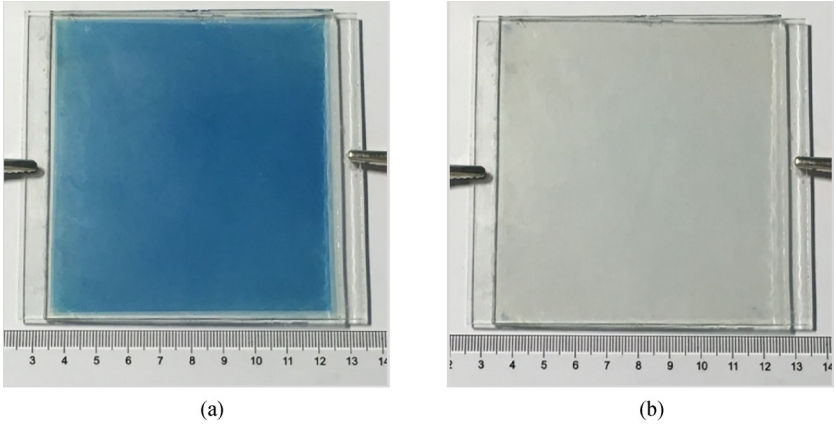

Fig. 5 (a) Coloration state of the large-area electrochromic device. (b) Bleaching state of the large-area electrochromic device

reaches a bright mode with high transmittance in the NIR and VIS ranges. However, the transmittance of the device rapidly decreases to zero in the band of more than 2000 nm owing to the effect of the FTO substrate. Under a voltage of –0.5 V, the electrochromic device reaches the cool mode, which blocks approximately 60% of NIR and ensures high transmittance in the VIS range. When a voltage of –2 V is applied, the VIS transmittance decreases considerably and the device reaches the dark mode (Fig. S12(b)). These results suggest that this smart window effectively modulates light transmission, which probably reduces the energy consumption of a building for refrigeration purpose. In addition, a flexible electrochromic device with a size of 3 cm × 3.5 cm exhibits a facile colored response during the bending state (Fig. S13). These results demonstrate the possibility of using this ink for practical applications as smart windows and flexible displays.

4 Conclusions

In summary, we successfully prepare a stable $Li_xNa_{2-x}W_4O_{13}$ nanosheet aqueous ink using the Li-ion exchange strategy. By exploiting the spray coating technology, the $Li_xNa_{2-x}W_4O_{13}$ nanosheet films are obtained on large-area rigid and flexible substrates in a low-cost, efficient, and environment-friendly manner. The complementary electrochromic device based on $Li_xNa_{2-x}W_4O_{13}$ nanosheet films exhibits large optical modulation (75% at 700 nm), fast switching responses (2/1.4 s), and outstanding cyclic stability (over 1000 cycles). This aqueous ink can be easily scaled up and exhibits broad application prospects in electrochromism, energy storage, and sensing. This study paves a new methodology to prepare other 2D ion-intercalated materials based on aqueous inks by appropriately selecting ion species.

Acknowledgements This work was financially supported by the National Natural Science Foundation of China (Grant Nos. 11874036, 51872101, 51672097, 51972124, and 51902115), the National Program for Support of Top-notch Young Professionals, the Program for HUST Academic Frontier Youth Team, the Fundamental Research Funds for the Central Universities (HUST: 2017KFXKJC001 and 2018KFYXKJC025), the Guangdong Province Key Area R&D Program (No. 2019B010940001), the Local Innovative and Research Teams Project of Guangdong Pearl River Talents Program (No. 2017BT01N111), and Basic Research Project of Shenzhen, China (No. JCYJ20170412171430026). We wish to thank the facility support from the Center for Nanoscale Characterization & Devices, WNLO of HUST and the Analytical and Testing Center of HUST.

Conflict of Interest The authors declare no conflict of interest.

Electronic Supplementary Material Supplementary material is available in the online version of this article at https://doi.org/10.1007/s12200-020-1033-z and is accessible for authorized users.

References

1. Baeg K J, Caironi M, Noh Y Y. Toward printed integrated circuits based on unipolar or ambipolar polymer semiconductors. Advanced Materials, 2013, 25(31): 4210–4244
2. Perelaer J, Smith P J, Mager D, Soltman D, Volkman S K, Subramanian V, Korvink J G, Schubert U S. Printed electronics: the challenges involved in printing devices, interconnects, and contacts based on inorganic materials. Journal of Materials Chemistry, 2010, 20(39): 8446–8453
3. Barrows A T, Pearson A J, Kwak C K, Dunbar A D F, Buckley A R, Lidzey D G. Efficient planar heterojunction mixed-halide perovskite solar cells deposited via spray-deposition. Energy & Environmental Science, 2014, 7(9): 2944–2950
4. Scardaci V, Coull R, Lyons P E, Rickard D, Coleman J N. Spray deposition of highly transparent, low-resistance networks of silver nanowires over large areas. Small, 2011, 7(18): 2621–2628
5. Sirringhaus H, Kawase T, Friend R H, Shimoda T, Inbasekaran M, Wu W, Woo E P. High-resolution inkjet printing of all-polymer transistor circuits. Science, 2000, 290(5499): 2123–2126
6. van Osch T H J, Perelaer J, de Laat A W M, Schubert U S. Inkjet printing of narrow conductive tracks on untreated polymeric substrates. Advanced Materials, 2008, 20(2): 343–345
7. Ding T, Liu K, Li J, Xue G, Chen Q, Huang L, Hu B, Zhou J. All-printed porous carbon film for electricity generation from evaporation-driven water flow. Advanced Functional Materials, 2017, 27(22): 1700551–1700555
8. Fang Y S, Wu Z C, Li J, Jiang F Y, Zhang K, Zhang Y L, Zhou Y H, Zhou J, Hu B. High-performance hazy silver nanowire transparent electrodes through diameter tailoring for semitransparent photovoltaics. Advanced Functional Materials, 2018, 28(9): 1705409–1705416
9. Kamyshny A, Magdassi S. Conductive nanomaterials for printed electronics. Small, 2014, 10(17): 3515–3535
10. Berggren M, Nilsson D, Robinson N D. Organic materials for printed electronics. Nature Materials, 2007, 6(1): 3–5
11. Bonaccorso F, Bartolotta A, Coleman J N, Backes C. 2D-crystal-based functional inks. Advanced Materials, 2016, 28(29): 6136–6166
12. Cai X, Luo Y, Liu B, Cheng H M. Preparation of 2D material dispersions and their applications. Chemical Society Reviews, 2018, 47(16): 6224–6266
13. Xiao X, Song H, Lin S, Zhou Y, Zhan X, Hu Z, Zhang Q, Sun J, Yang B, Li T, Jiao L, Zhou J, Tang J, Gogotsi Y. Scalable salt-templated synthesis of two-dimensional transition metal oxides. Nature Communications, 2016, 7(1): 11296–11303
14. Hu Z, Xiao X, Jin H, Li T, Chen M, Liang Z, Guo Z, Li J, Wan J, Huang L, Zhang Y, Feng G, Zhou J. Rapid mass production of two-dimensional metal oxides and hydroxides via the molten salts method. Nature Communications, 2017, 8(1): 15630–15638
15. Zhao Y, Zhu K. Efficient planar perovskite solar cells based on 1.8 eV band gap $CH_3NH_3PbI_2Br$ nanosheets via thermal decomposition. Journal of the American Chemical Society, 2014, 136(35): 12241–12244
16. Pospischil A, Furchi M M, Mueller T. Solar-energy conversion and light emission in an atomic monolayer p-n diode. Nature Nanotechnology, 2014, 9(4): 257–261
17. Li T, Jin H, Liang Z, Huang L, Lu Y, Yu H, Hu Z, Wu J, Xia B Y, Feng G, Zhou J. Synthesis of single crystalline two-dimensional transition-metal phosphides via a salt-templating method. Nanoscale, 2018, 10(15): 6844–6849
18. Chen Z, Song Y, Cai J, Zheng X, Han D, Wu Y, Zang Y, Niu S, Liu Y, Zhu J, Liu X, Wang G. Tailoring the d-band centers enables Co_4N nanosheets to be highly active for hydrogen evolution catalysis. Angewandte Chemie International Edition, 2018, 57(18): 5076–5080
19. Kelly A G, Hallam T, Backes C, Harvey A, Esmaeily A S, Godwin I, Coelho J, Nicolosi V, Lauth J, Kulkarni A, Kinge S, Siebbeles L D A, Duesberg G S, Coleman J N. All-printed thin-film transistors from networks of liquid-exfoliated nanosheets. Science, 2017, 356(6333): 69–73
20. Withers F, Yang H, Britnell L, Rooney A P, Lewis E, Felten A, Woods C R, Sanchez Romaguera V, Georgiou T, Eckmann A, Kim Y J, Yeates S G, Haigh S J, Geim A K, Novoselov K S, Casiraghi C. Heterostructures produced from nanosheet-based inks. Nano Letters, 2014, 14(7): 3987–3992

21. Zhang C J, Kremer M P, Seral-Ascaso A, Park S H, McEvoy N, Anasori B, Gogotsi Y, Nicolosi V. Stamping of flexible, coplanar micro-supercapacitors using MXene inks. Advanced Functional Materials, 2018, 28(9): 1705506–1705515
22. Bie Y Q, Grosso G, Heuck M, Furchi M M, Cao Y, Zheng J, Bunandar D, Navarro-Moratalla E, Zhou L, Efetov D K, Taniguchi T, Watanabe K, Kong J, Englund D, Jarillo-Herrero P. A $MoTe_2$-based light-emitting diode and photodetector for silicon photonic integrated circuits. Nature Nanotechnology, 2017, 12(12): 1124–1129
23. Hernandez Y, Nicolosi V, Lotya M, Blighe F M, Sun Z, De S, McGovern I T, Holland B, Byrne M, Gun'Ko Y K, Boland J J, Niraj P, Duesberg G, Krishnamurthy S, Goodhue R, Hutchison J, Scardaci V, Ferrari A C, Coleman J N. High-yield production of graphene by liquid-phase exfoliation of graphite. Nature Nanotechnology, 2008, 3(9): 563–568
24. Mashtalir O, Naguib M, Mochalin V N, Dall'Agnese Y, Heon M, Barsoum M W, Gogotsi Y. Intercalation and delamination of layered carbides and carbonitrides. Nature Communications, 2013, 4(1): 1716–1722
25. Coleman J N, Lotya M, O'Neill A, Bergin S D, King P J, Khan U, Young K, Gaucher A, De S, Smith R J, Shvets I V, Arora S K, Stanton G, Kim H Y, Lee K, Kim G T, Duesberg G S, Hallam T, Boland J J, Wang J J, Donegan J F, Grunlan J C, Moriarty G, Shmeliov A, Nicholls R J, Perkins J M, Grieveson E M, Theuwissen K, McComb D W, Nellist P D, Nicolosi V. Two-dimensional nanosheets produced by liquid exfoliation of layered materials. Science, 2011, 331(6017): 568–571
26. Mendoza-Sánchez B, Hanlon D, Coelho J, Brien S O, Pettersson H. An investigation of the energy storage properties of a 2D α-MoO_3-SWCNTs composite films. 2D Materials, 2016, 4(1): 015005–015012
27. Lin S, Shih C J, Strano M S, Blankschtein D. Molecular insights into the surface morphology, layering structure, and aggregation kinetics of surfactant-stabilized graphene dispersions. Journal of the American Chemical Society, 2011, 133(32): 12810–12823
28. Wang J L, Lu Y R, Li H H, Liu J W, Yu S H. Large area co-assembly of nanowires for flexible transparent smart windows. Journal of the American Chemical Society, 2017, 139(29): 9921–9926
29. Cong S, Tian Y, Li Q, Zhao Z, Geng F. Single-crystalline tungsten oxide quantum dots for fast pseudocapacitor and electrochromic applications. Advanced Materials, 2014, 26(25): 4260–4267
30. Shendage S S, Patil V L, Vanalakar S A, Patil S P, Harale N S, Bhosale J L, Kim J H, Patil P S. Sensitive and selective NO_2 gas sensor based on WO_3 nanoplates. Sensors and Actuators B, Chemical, 2017, 240: 426–433
31. Sun S, Watanabe M, Wu J, An Q, Ishihara T. Ultrathin $WO_3 \cdot 0.33H_2O$ nanotubes for CO_2 photoreduction to acetate with high selectivity. Journal of the American Chemical Society, 2018, 140(20): 6474–6482
32. Liang L, Li K, Xiao C, Fan S, Liu J, Zhang W, Xu W, Tong W, Liao J, Zhou Y, Ye B, Xie Y. Vacancy associates-rich ultrathin nanosheets for high performance and flexible nonvolatile memory device. Journal of the American Chemical Society, 2015, 137(8): 3102–3108
33. Wang J, Zhang L, Yu L, Jiao Z, Xie H, Lou X W, Sun X W. A bi-functional device for self-powered electrochromic window and self-rechargeable transparent battery applications. Nature Communications, 2014, 5(1): 4921–4927
34. Kresse G, Furthmüller J. Efficient iterative schemes for *ab initio* total-energy calculations using a plane-wave basis set. Physical Review B, 1996, 54(16): 11169–11186
35. Kresse G, Furthmüller J. Efficiency of ab-initio total energy calculations for metals and semiconductors using a plane-wave basis set. Computational Materials Science, 1996, 6(1): 15–50
36. Blöchl P E. Projector augmented-wave method. Physical Review B, 1994, 50(24): 17953–17979
37. Perdew J P, Burke K, Ernzerhof M. Generialized gradient approximation made simple. Physical Review Letters, 1996, 77 (18): 3865–3868
38. Mathew K, Sundararaman R, Letchworth-Weaver K, Arias T A, Hennig R G. Implicit solvation model for density-functional study of nanocrystal surfaces and reaction pathways. Journal of Chemical Physics, 2014, 140(8): 084106–084113
39. Kim J, Kwon S, Cho D H, Kang B, Kwon H, Kim Y, Park S O, Jung G Y, Shin E, Kim W G, Lee H, Ryu G H, Choi M, Kim T H, Oh J, Park S, Kwak S K, Yoon S W, Byun D, Lee Z, Lee C. Direct exfoliation and dispersion of two-dimensional materials in pure water via temperature control. Nature Communications, 2015, 6(1): 8294–8302
40. Smith R J, Lotya M, Coleman J N. The importance of repulsive potential barriers for the dispersion of graphene using surfactants. New Journal of Physics, 2010, 12(12): 125008–125018
41. Jiao Z, Wang J, Ke L, Liu X, Demir H V, Yang M F, Sun X W. Electrochromic properties of nanostructured tungsten trioxide (hydrate) films and their applications in a complementary electrochromic device. Electrochimica Acta, 2012, 63: 153–160
42. Van der Ven A, Thomas J C, Xu Q, Bhattacharya J. Linking the electronic structure of solids to their thermodynamic and kinetic properties. Mathematics and Computers in Simulation, 2010, 80(7): 1393–1410
43. Van der Ven A, Thomas J C, Xu Q, Swoboda B, Morgan D. Nondilute diffusion from first principles: Li diffusion in Li_xTiS_2. Physical Review B, 2008, 78(10): 104306
44. Cai G, Darmawan P, Cheng X, Lee P S. Inkjet printed large area multifunctional smart windows. Advanced Energy Materials, 2017, 7(14): 1602598–1602605
45. Liang L, Zhang J, Zhou Y, Xie J, Zhang X, Guan M, Pan B, Xie Y. High-performance flexible electrochromic device based on facile semiconductor-to-metal transition realized by $WO_3 \cdot 2H_2O$ ultrathin nanosheets. Scientific Reports, 2013, 3(1): 1936–1943
46. Azam A, Kim J, Park J, Novak T G, Tiwari A P, Song S H, Kim B, Jeon S. Two-dimensional WO_3 nanosheets chemically converted from layered WS_2 for high-performance electrochromic devices. Nano Letters, 2018, 18(9): 5646–5651
47. Yang P, Sun P, Chai Z, Huang L, Cai X, Tan S, Song J, Mai W. Large-scale fabrication of pseudocapacitive glass windows that combine electrochromism and energy storage. Angewandte Chemie International Edition, 2014, 53(44): 11935–11939
48. Granqvist C G. Electrochromics for smart windows: oxide-based thin films and devices. Thin Solid Films, 2014, 564: 1–38
49. Llordés A, Garcia G, Gazquez J, Milliron D J. Tunable near-infrared

and visible-light transmittance in nanocrystal-in-glass composites. Nature, 2013, 500(7462): 323–326

50. Zhang S, Cao S, Zhang T, Fisher A, Lee J Y. Al^{3+} intercalation/de-intercalation-enabled dual-band electrochromic smart windows with a high optical modulation, quick response and long cycle life. Energy & Environmental Science, 2018, 11(10): 2884–2892

Jia Li obtained his Ph.D. degree from Tsinghua University in 2009. Then he was a Postdoctoral Research Fellow in Fritz Haber Institute of the Max Planck Society in Berlin, Germany from 2009 to 2010. He is currently an associate professor of Tsinghua Shenzhen International Graduate School, Tsinghua University. His research interest is applying first-principles methods to study the relationship between the structure and the performance of energy storage and conversion for two-dimensional materials.

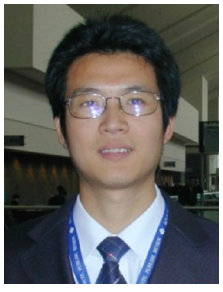

Jun Zhou is a professor in Wuhan National Laboratory for Optoelectronics at Huazhong University of Science and Technology. He received his bachelor degree (2001) in materials physics and Ph.D. degree (2007) in materials physics and chemistry from the Sun Yat-sen University. He was a visiting student (2005–2006), a research scientist (2007–2009) in Georgia Institute of Technology. His recent research interest is energy harvesting materials and devices.

Supporting Information

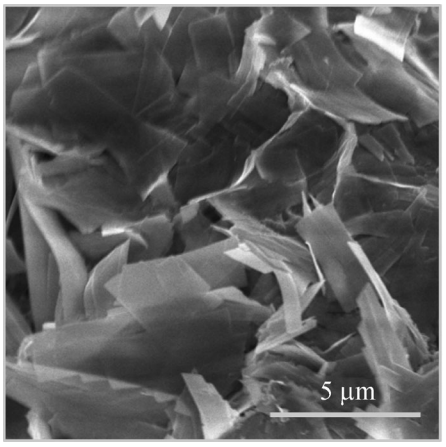

Fig. S1 SEM image of the $Na_2W_4O_{13}$ nanosheets synthesized using the molten salt method

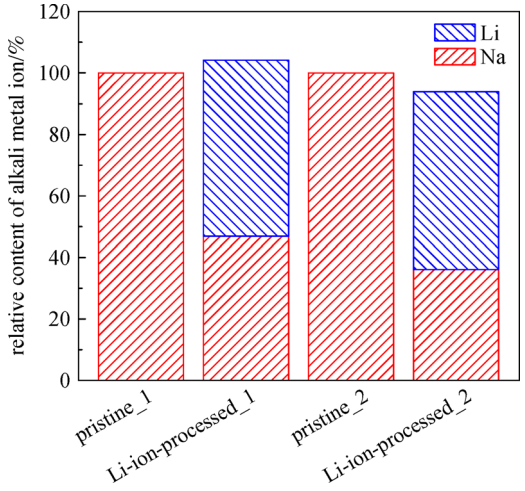

Fig. S2 Content of the alkali metal ion in pristine and Li-ion-exchanged samples

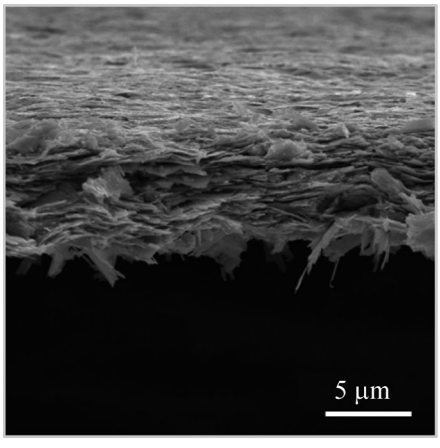

Fig. S3 Cross-sectional SEM image of the $Li_xNa_{2-x}W_4O_{13}$ nanosheets collected by vacuum filtration

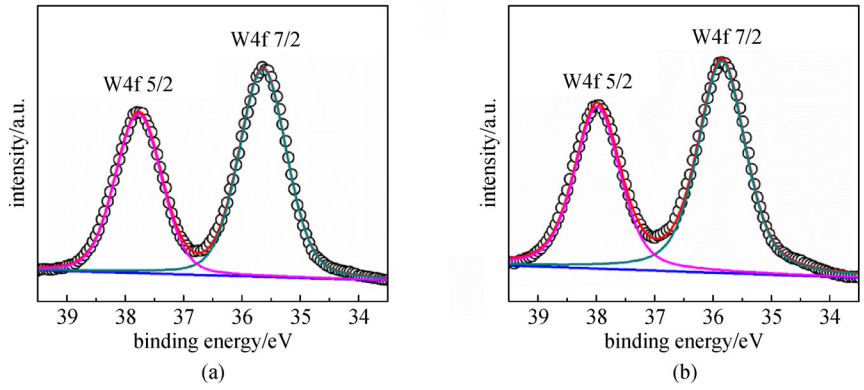

Fig. S4 W4f region XPS spectra of (a) $Li_xNa_{2-x}W_4O_{13}$ nanosheets and (b) $Na_2W_4O_{13}$ nanosheets

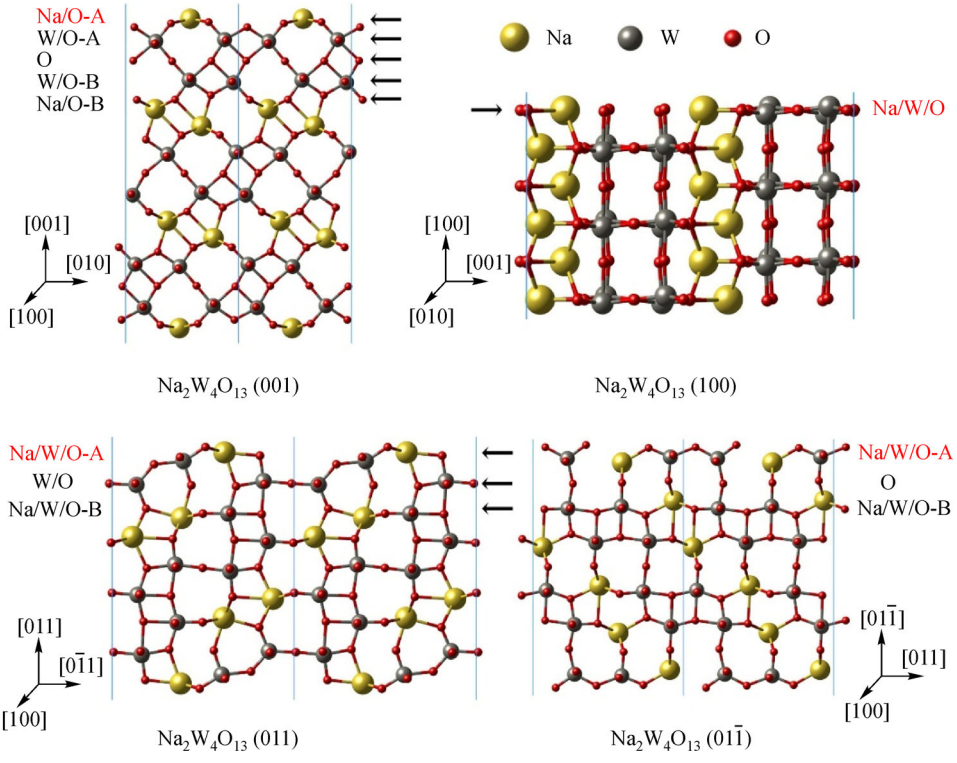

Fig. S5 Different terminations of the (001), (100), (011), and (01$\bar{1}$) facets of $Na_2W_4O_{13}$. Yellow, dark gray, and red spheres denote the sodium, tungsten, and oxygen atoms, respectively

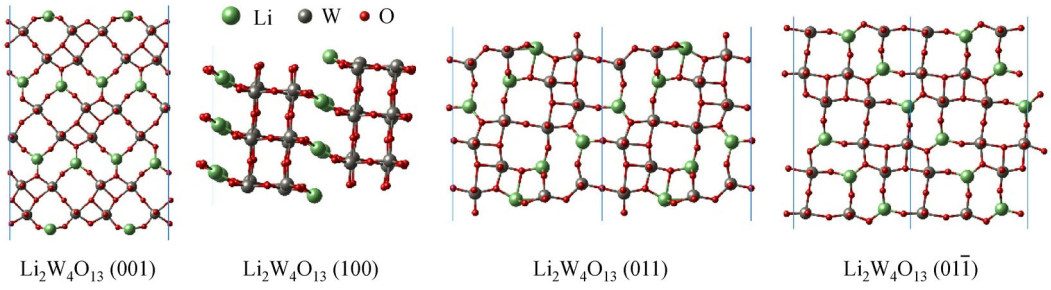

Fig. S6 Favorable terminations of the (001), (100), (011), and (01$\bar{1}$) facets of $Li_2W_4O_{13}$. Green, dark gray, and red circles denote the sodium, tungsten, and oxygen atoms, respectively

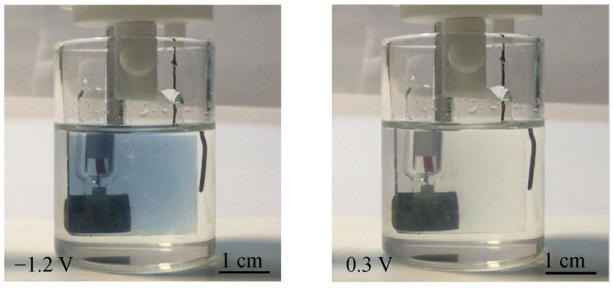

Fig. S7 (a) Coloration state of the $Li_xNa_{2-x}W_4O_{13}$ nanosheet film under a potential of –1.2 V. (b) Bleaching state of the $Li_xNa_{2-x}W_4O_{13}$ nanosheet film under a potential of 0.3 V

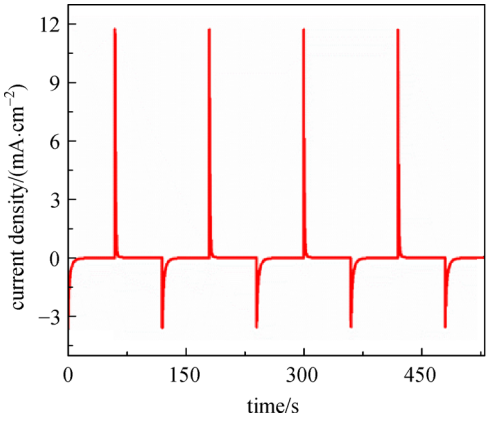

Fig. S8 *In situ* chronoamperometric transients for the $Li_xNa_{2-x}W_4O_{13}$ nanosheet film during the electrochromic process

Table S1 Calculated surface energies of different terminations for the (001), (100), (011), and (01$\bar{1}$) facets of $Na_2W_4O_{13}$. The notations of the termination structure are defined in Fig. S5

surface	termination	γ/(J·m^{-2})
(001)	Na/O-A	0.165
	W/O-A	2.719
	O	2.427
	W/O-B	7.605
	Na/O-B	4.165
(100)	Na/W/O	0.799
(011)	Na/W/O-A	0.430
	W/O	2.304
	Na/W/O-B	0.802
(01$\bar{1}$)	Na/W/O-A	0.408
	O	1.612
	Na/W/O-B	2.754

Table S2 Calculated interfacial energies of the (001), (100), (011), and (01$\bar{1}$) facets of $Na_2W_4O_{13}$ and $Li_2W_4O_{13}$ with favorable terminations in water

compound	surface	$\gamma_{interface}$/(J·m^{-2})
$Na_2W_4O_{13}$	(001)	−0.360
	(100)	0.351
	(011)	0.029
	(01$\bar{1}$)	−0.101
$Li_2W_4O_{13}$	(001)	−1.112
	(100)	−0.108
	(011)	−0.091
	(01$\bar{1}$)	−0.468

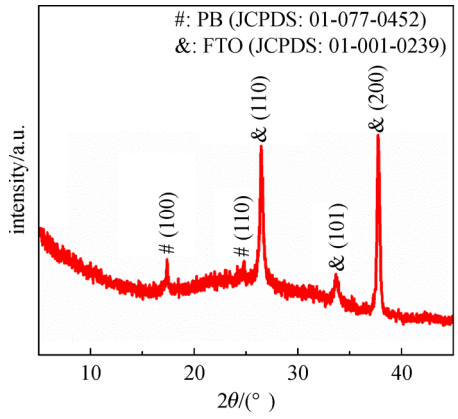

Fig. S9 XRD pattern of the PB film on FTO glass

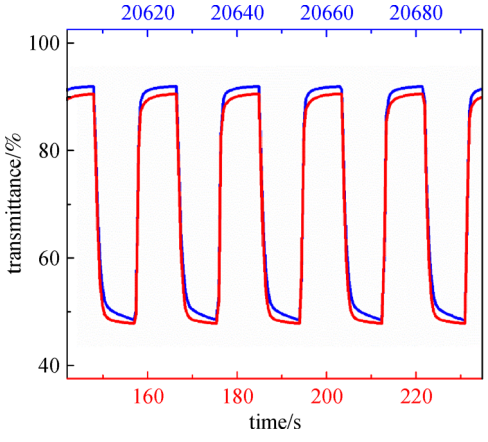

Fig. S10 Detailed *in situ* optical transmittance at 550 nm for measuring the cyclic stability (red: first several cycles, blue: after 1000 cycles)

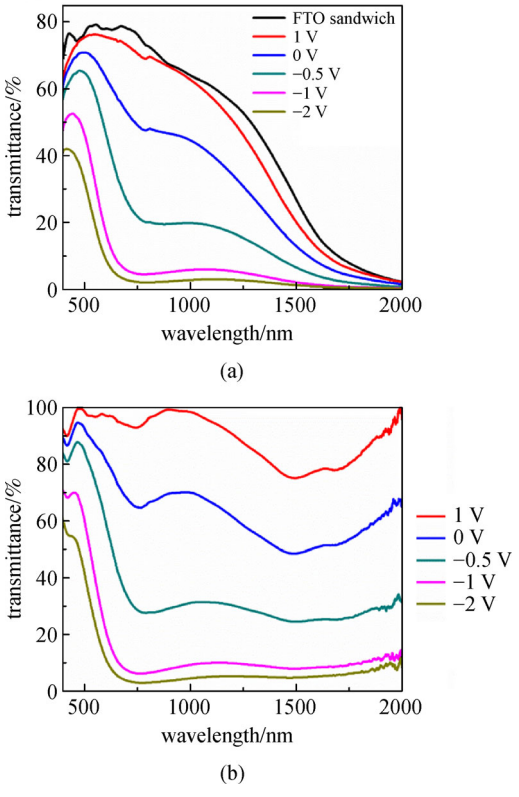

Fig. S12 (a) Transmittance spectrum of the prototype electrochromic device under different voltages. (b) Relative transmittance spectrum of the prototype electrochromic device (two FTO glasses sandwiching the electrolyte as a baseline)

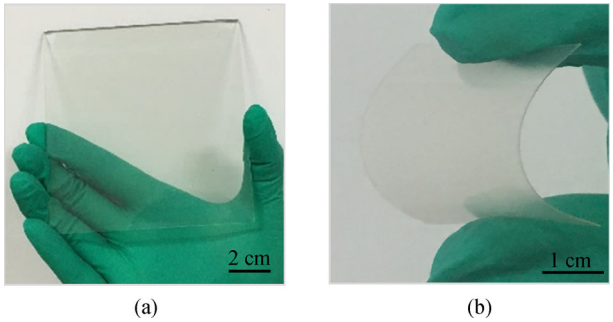

Fig. S11 (a) Photograph of the large-area $Li_xNa_{2-x}W_4O_{13}$ nanosheet film (9 cm × 10 cm) sprayed on the FTO glass. (b) Photograph of the $Li_xNa_{2-x}W_4O_{13}$ nanosheet film (3 cm × 3.5 cm) sprayed on a flexible ITO substrate

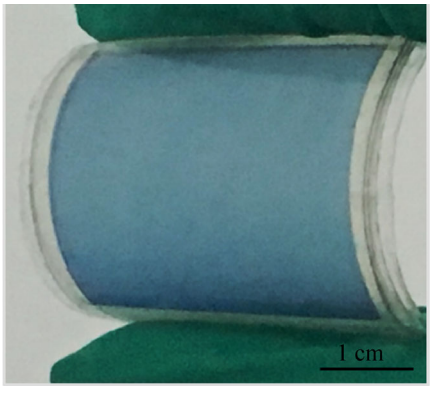

Fig. S13 Coloration state of the flexible electrochromic device